ADVANCED ENERGY MATERIALS
www.advenergymat.de

High-Throughput Screening of High-Entropy Fluorite-Type Oxides as Potential Candidates for Photovoltaic Applications

Mukesh Kumbhakar, Anurag Khandelwal, Shikhar Krishn Jha, Monaha Veerraju Kante, Pirmin Keßler, Uli Lemmer, Horst Hahn, Jasmin Aghassi-Hagmann, Alexander Colsmann, Ben Breitung, Leonardo Velasco,* and Simon Schweidler**

High-throughput (HT) synthesis and HT characterization techniques are becoming increasingly important due to the ever-increasing complexity of materials and applications of advanced functional compounds. This work reports on the high-throughput compilation of material libraries of high-entropy oxides with fluorite crystal structure and tunable band gaps to be used as, e.g., semiconductors for photovoltaic applications. The material libraries cover the high-entropy range of rare-earth oxides with 5, 6, and 7 different cations (Ce, La, Sm, Pr, Tb, Y, and Zr) in near equimolar concentrations, but also the medium entropy range with 4 cations. The atmosphere used during or after synthesis is found to have a large effect on the band gap of these materials. Multivalent rare-earth cations such as Ce/Pr/Tb enable reversible tuning of the band gap between 2.0 and 3.5 eV upon calcination under various oxidizing and reducing atmospheres. The high-entropy fluorite oxides with smaller band gaps exhibit high electron mobility and transport energy levels compatible with common solar cell architectures.

1. Introduction

The introduction of the high-entropy concept to material design has enabled unique approaches to the development of new functional materials.[1,2,11,12,3–10] The high-entropy concept describes the strategy to include many different elements into a single-phase structure, therefore increasing the configurational entropy, in order to achieve various properties stemming from the so-called cocktail effects and lattice distortions.[13,14] The combination of possible entropy stabilization, cocktail effects, and lattice distortion enables the tailoring of the structure and functionality of materials and to obtain unprecedented and exciting properties. Whenever the crystal structure has a strong correlation to the material properties of interest, the introduction of high entropy can be utilized to modify these.

M. Kumbhakar, S. K. Jha
Department of Materials Science and Engineering
Indian Institute of Technology Kanpur
Kanpur 208016, India

A. Khandelwal, M. V. Kante, H. Hahn, J. Aghassi-Hagmann, B. Breitung, S. Schweidler
Institute of Nanotechnology
Karlsruhe Institute of Technology
Hermann-von-Helmholtz-Platz 1, 76344 Eggenstein Leopoldshafen, Germany
E-mail: ben.breitung@kit.edu; simon.schweidler@kit.edu

P. Keßler, U. Lemmer
Light Technology Institute
Karlsruhe Institute of Technology
76131 Karlsruhe, Germany

P. Keßler, U. Lemmer
Institute of Microstructure Technology
Karlsruhe Institute of Technology
76344 Eggenstein-Leopoldshafen, Germany

H. Hahn
School of Chemical
Biological
and Materials Engineering
The University of Oklahoma
Norman, OK 73019, USA

A. Colsmann
Material Research Center for Energy Systems
Karlsruhe Institute of Technology
Strasse am Forum 7, 76131 Karlsruhe, Germany

L. Velasco
Universidad Nacional de Colombia sede de La Paz
Km 9 via Valledupar, La Paz, Cesar 202010, Colombia
E-mail: lvelascoe@unal.edu.co

The ORCID identification number(s) for the author(s) of this article can be found under https://doi.org/10.1002/aenm.202204337

DOI: 10.1002/aenm.202204337

So far, new high-entropy materials have mostly been developed on a trial-and-error basis. Given a large number of possible combinations for high-entropy compositions, including variations of the elemental composition as well as the stoichiometry, the trial-and-error approach alone is far too slow and inefficient for controlled tailoring of material properties. Therefore, theoretical approaches have been developed to predict the properties of high-entropy materials, but the lack of well-defined unit cells and a large number of variables make it difficult to accurately model this emerging class of materials.[15,16] It is expected that a more effective optimization and development of high-entropy materials can be achieved by combining theoretical and high-throughput experimental methods. The first step in this direction is to develop appropriate high-throughput synthesis and characterization methods and link the results to a desired application.[17–22]

In this work, we carried out a case study on high-throughput synthesis and characterization of fluorite-type oxides to generate data sets for material libraries and to identify potential application areas such as novel light collection material for photovoltaic applications. Oxides with fluorite structure are an emerging class of materials that offer many promising properties for a wide range of electronics and energy applications.[23–28] In particular, the ability to achieve semiconducting properties in certain compositions makes them attractive for energy and optoelectronic applications. Here, we deliberately populated the cation site of the crystal stepwise with an equimolar choice of up to seven rare-earth (RE) metals, therefore entering the realm of high-entropy materials with a configurational entropy of $>1.5R$ (R being the ideal gas constant). Different thermal treatments and atmospheres added to the huge parameter space. Yet, automation allowed the consistent and fast identification of suitable compounds with optical band gaps in the visible spectrum.

2. Results and Discussion

2.1. Choice of Materials

This study focuses on high-throughput synthesis and characterization of medium-entropy and high-entropy fluorite-type oxides with a combination of 4, 5, 6, or 7 different cations (Ce, La, Sm, Pr, Tb, Y, and Zr). The band gap of these materials was modified by different heat treatments, and material libraries were prepared with the band gap energy as the identifying parameter. From these material libraries, some fluorite oxides with promising band gaps were selected, and the ionization potential (IP) was evaluated by photoelectron spectroscopy in air (PESA) and Hall-effect measurements. The idea of using rare-earth fluorite-type oxides for high-entropy material design is leveraged by several earlier studies that have shown that the band gap energy of rare-earth oxides (REO), such as CeO_2, can be modified by doping while maintaining their crystal structure.[5,23,29]

A total of 64 different medium- and high-entropy rare-earth fluorite-type oxides were synthesized using an automated pipetting robot followed by calcination. For this purpose, the chosen cations were mixed in different equimolar ratios, resulting in quaternary compositions (35 samples, configurational entropy $S_{config} = 1.39R$), quinary compositions (21 samples, $S_{config} = 1.61R$), senary compositions (7 samples, $S_{config} = 1.79R$), and one septenary combination (1 sample, $S_{config} = 1.95R$). **Figure 1**a,b shows S_{config} at 700 and 900 °C, respectively. The diagrams can be understood as follows: The material with 7 different cations $(CeLaPrSmYZrTb)O_2$ is represented by the point in the middle. Following the straight lines, the indicated cation is removed from this composition. This results in 6 cation compositions in the first cycle, 5 cation compositions in the second cycle, and 4 cation compositions in the third cycle. Accordingly, the S_{config} of the composition is reduced from the center outward.

2.2. Crystallographic Analysis

Since single-phase materials are preferred for optoelectronic applications with tailored properties, the samples were next characterized by high-throughput XRD and SEM/EDX measurements, and the crystal phases are indicated in Figure 1a,b with symbols. For a better visibility, Figure 1c,d shows color-coded graphs representing the crystal phases. All data is also summarized in Tables S1 and S2 (Supporting Information). The XRD analysis shows that the majority of the multicomponent materials at the calcination temperatures of 700 and 900 °C have a single-phase fluorite-type structure (space group = *Fm*-3*m*), accounting for 66% (42 combinations) and 63% (40 combinations) of all possible combinations, respectively. Although the difference here is marginal, this observation is surprising since the higher calcination temperature initially lets us expect an increase in the formation of phase-pure single compounds, as reported for high-entropy oxides. Yet, a more detailed investigation of the different phases revealed possible effects of individual cations or cation combinations on the crystal structure formation. For example, in multicomponent rare-earth fluorite oxides, the two +4 cations Ce and Zr may stabilize the fluorite structure while the other cations are incorporated into the existing matrix. Nevertheless, Figure 1 shows that even some systems that do not contain Ce or Zr form a single-phase *Fm*-3*m* structure. This is in contrast to earlier results and assumptions in the literature.[5,6,16,23,29] In 4-cation systems, the absence of Ce, Zr, and one other element, or the absence of Zr in combination with one or two multivalent cations (Tb and Pr), appears to favor the formation of a single bixbyite (*Ia*-3) phase. For example, the materials $(CeLaSmY)O_2$, $(LaSmPrY)O_2$, and $(SmPrYTb)O_2$ crystallize in the *Ia*-3 crystal structure independently of the calcination temperature (700 and 900 °C). While the composition $(LaSmYTb)O_2$, $(LaPrYTb)O_2$, and $(CeSmYTb)O_2$, at 700 and 900 °C show a phase change from bixbyite phase to multiphase phase (unknown phases), bixbyite phase to multiphase (two fluorite phases) and fluorite phase to bixbyite phase. However, it appears that the noninclusion of Ce and the inclusion of Tb favors the formation of a multiple *Fm*-3*m* phase. We note that "multiple phase *Fm*-3*m*" represents several fluorite-type phases with slightly different lattice parameters without reference to various other phases (Figure 1; Tables S1 and S2, Supporting Information). Depending on the composition, the percentage of the secondary phase varies in a range of about 10–35 wt% (Tables S1 and S2, Supporting Information). Other effects were also observed; an overview of the effect of the different elements on the phase formations is listed in **Table 1**.

We note that all 7- and 6-cation compounds with configurational entropies beyond $1.7R$ exhibit a single *Fm*-3*m* crystal structure at both calcination temperatures. Only when the

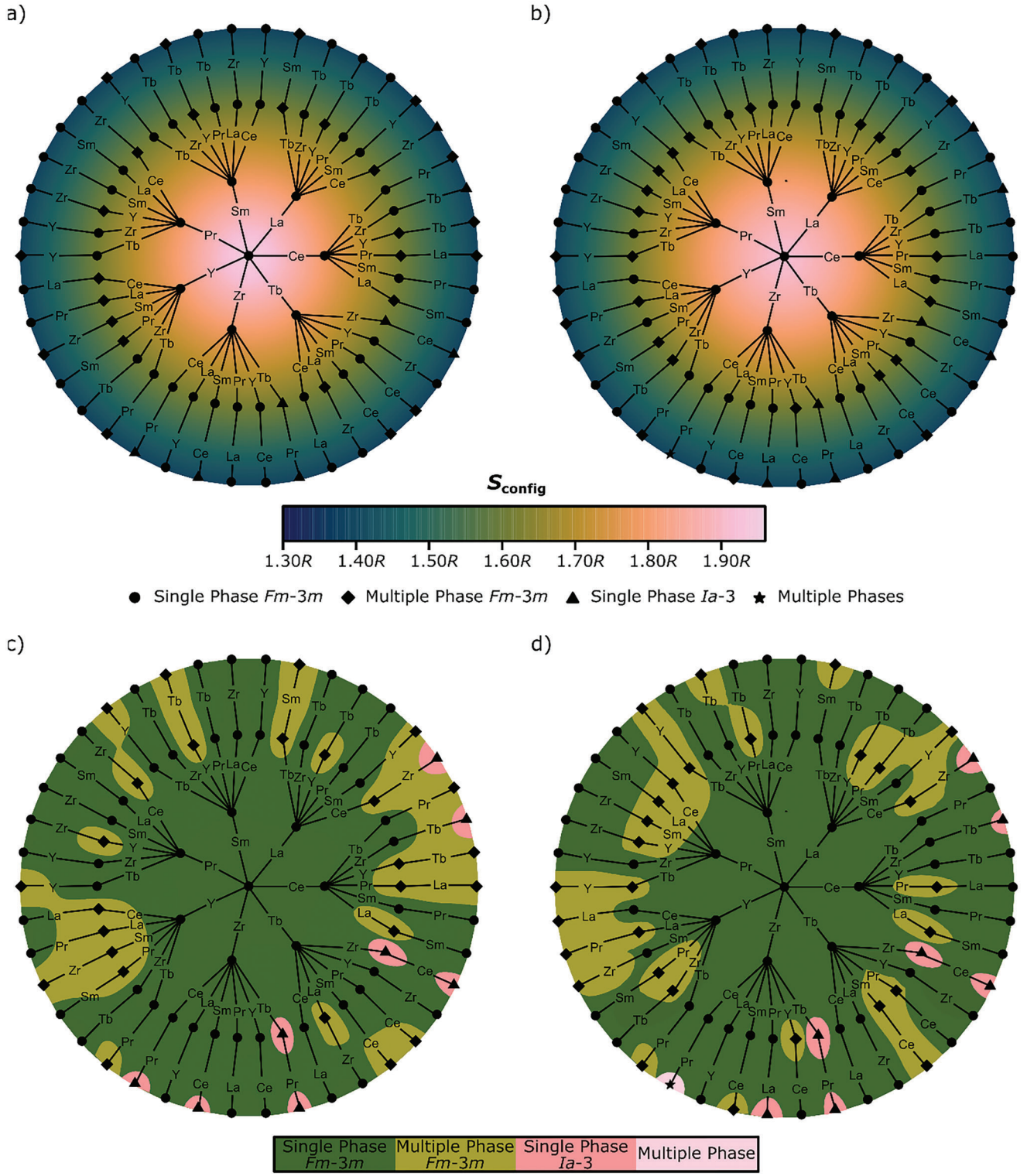

Figure 1. a) Contour plot of S_{config} of the rare-earth oxides calcinated at 700 °C and b) at 900 °C. Symbols represent the crystal phases. c) Color-coded phases of each sample after calcination at 700 °C and d) 900 °C for better visibility. We note that some compositions are duplicated in this type of chart. "Multiple phase *Fm*-3*m*" means that multiple fluorite phases with slightly different lattice parameters were visible in the XRD data.

Table 1. Effect of different cations and cation combinations on the phase formation. Cations with the prefix "–" are removed, and cations without a prefix are contained in the crystal structure.

Cation combination	Effect
–Zr	More likely to form single-phase *Fm*-3*m*
Zr, –Tb	*Fm*-3*m*, multiple phases
–Ce, –Zr, –Tb/Pr	*Ia*-3 phase
Tb, –Ce	Multiple phases

configurational entropy is reduced by subtracting elements that transition to a 5- or 4-cationic system do multiple phases or phase changes occur. We assume that due to the high-entropy theory, where a large configurational entropy can compensate for the enthalpy of mixing and counteract phase separations, a large number of different cations contributes to the stabilization of the *Fm*-3*m* crystal structure.[13,14] For materials with a configurational entropy below 1.7*R*, no conclusion on the phase stability can be drawn.

2.3. Optical Band Gap

Solar applications require materials that can harvest substantial parts of the visible spectrum. While most oxides exhibit rather wide band gaps, here, we target materials with narrow-to-intermediate band gaps. Thus, the absorption spectra of the 64 rare-earth oxide compositions are characterized in reflection geometry on powders using a custom-built XYZ robot equipped with a UV–vis detector. Rare-earth fluorite-type oxides were chosen as suitable materials because several studies have already shown that the band gap energy of rare-earth oxides such as CeO_2 can be modified by doping or different atmospheres and temperatures during calcination while maintaining the *Fm*-3*m* structure.[5,23,29] For such materials, it was found that, in particular, the presence of Pr and Tb (in the +3/+4 state) leads to the formation of intermediate 4f energy levels between the O 2p and rare-earth (RE) 5d gaps and therefore has a strong impact on the band gap.[5,23,29] The data obtained (5 measurements per sample, a total of 320 measurements) were automatically evaluated using a Python script. The automated data acquisition and evaluation thus allow relatively time-efficient creation of material libraries and contour plots (**Figures 2** and **3**), which facilitate the selection of suitable materials. The contour plots in Figure 2 show the band gap energies of the different compositions at both calcination temperatures (700 and 900 °C). A tabular comparison of the band gap energies is provided in Table S3 (Supporting Information). Notably, the trend of the band gap energies (Figure 2) of each compound after calcination at 700 and 900 °C are similar. While the band gap energies of most materials calcinated at 900 °C are slightly lower, $(CeSmPrY)O_2$ exhibited a significantly higher band gap energy at 900 °C, which is quite surprising since a higher calcination temperature commonly leads to a minimization of the band gap.

$(CeLaSmY)O_2$, $(CeLaSmZr)O_2$, $(CeLaYZr)O_2$, $(CeSmYZr)O_2$, $(LaSmYZr)O_2$, and $(CeLaSmYZr)O_2$ exhibited the widest band gap (3.0–4.9 eV). Notably, all materials with such a high band gap energy (3.0–4.9 eV) contain neither Pr nor Tb (Figure 2c).

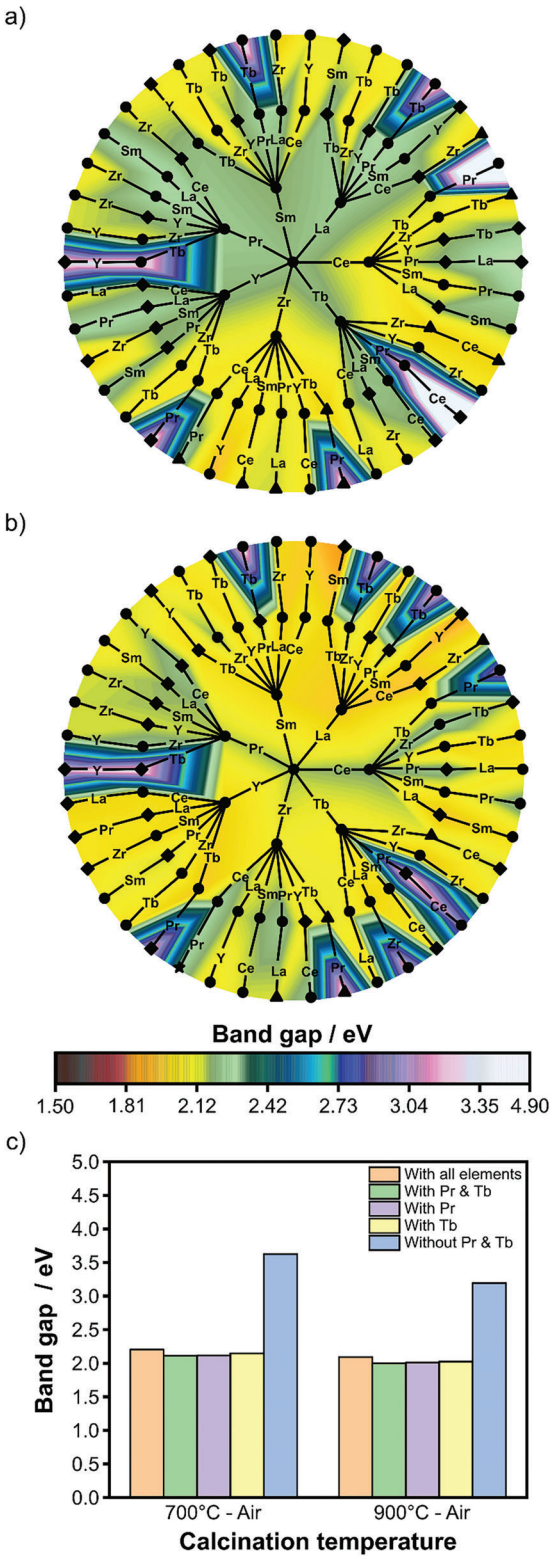

Figure 2. Contour plots of the band gap energies of the REOs calcinated at a) 700 °C and b) 900 °C in air. c) Influence of the cations on the band gap energy. The symbols in (a) and (b) are the same as in Figure 1; the bullet point stands for single phase *Fm-3m*, the square for multiple *Fm-3m* phases, the triangle for *Ia-3* phases and the star for multiple different phases.

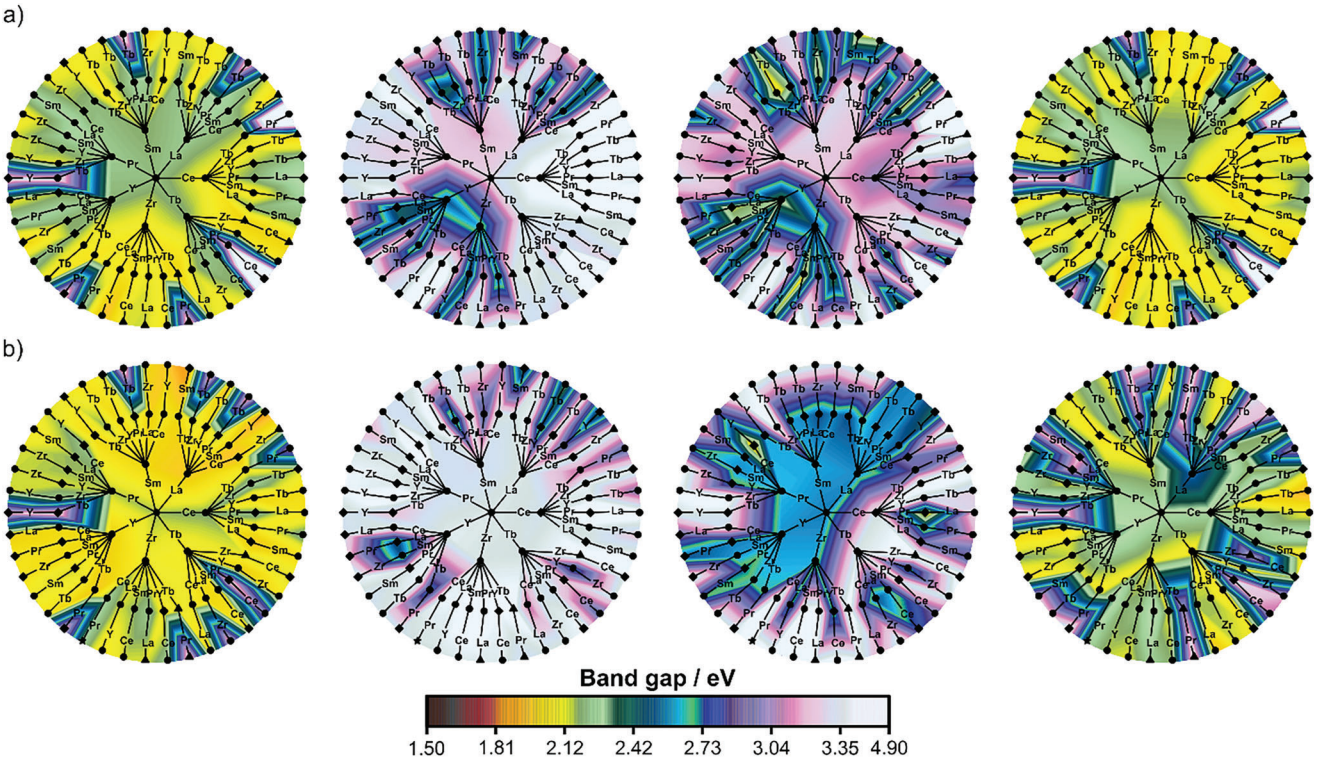

Figure 3. Contour plots of the band gap energies of the REOs at a) 700 °C and b) 900 °C. From left to right, the atmosphere in which the calcination was performed changes from air to argon to 10% H_2/argon and back to air.

In contrast, all other material compositions containing Pr, Tb or both have significantly lower band gap energies. This behavior fits well with previous reports, e.g., doping studies of various oxides, where the presence of different multivalent cations had a large effect on the band gap energy.[5,23,30–32] Changes in the band gap generally may be triggered, for example, by point defects (oxygen defects) or changes in the oxidation states of the incorporated elements, which consequently change the electronic structure.[25,33–39] Here, we rule out the formation of oxygen defects as the main reason for the observed large changes since oxygen defects typically produce band gap narrowing on the order of ≈0.3 eV only. We rather attribute the band gap change to the occupation of the RE 4f energy bands, which are formed between the O 2p and RE 5d energy levels. The occupied and unoccupied RE 4f band energies located between the oxygen 2p and RE 5d energy levels may vary due to the incorporation of different RE elements. In other words, for most REOs, the band gap energies refer to the electronic transitions from the O 2p to the RE 5d or RE 5d + $4f_{unoccupied}$. The latter is relevant when the unoccupied 4f bands lie between O 2p and RE 5d. For example, considering CeO_2 (band gap = 3.2 eV) as a reference system, we find that an additional 4f band between O 2p and Ce 4f, due to substitution by Pr and/or Tb, is associated with a decrease in the band gap to about 2 eV. This assumption, which can be applied to high and intermediate entropy REOs and has already been studied in some materials, is consistent with the band gap energies we observed (Figure 2) in all 64 REO compositions. The strong influence of Pr and Tb on the band gap reduction is evident upon a comparison of the materials with and without Pr and/or Tb in Figure 2c.

2.4. Calcination Atmosphere

In addition to the calcination temperature, the atmosphere during calcination plays an important role in setting the band gap. Earlier studies have shown that the band gap energy of REOs, such as CeO_2, can be modified by different atmospheres and temperatures during calcination while maintaining the *Fm*-3*m* crystal structure.[5,23,29] To adjust the optical properties, the very same samples were calcinated in the following order: i) air, ii) argon, iii) 10% H_2/argon, and iv) air, at either 700 or 900 °C (Figure 3), and characterized for their band gaps in-between these calcination processes. Different reducing or oxidizing atmospheres were used to selectively change the occupancies of the 4f states of the multivalent Pr^{3+}/Pr^{4+} and Tb^{3+}/Tb^{4+}.[5,23]

As depicted in Figure 3 and Tables S4 and S5 (Supporting Information), calcination in different atmospheres lead to strong changes in the band gap. Treatment in argon and H_2/argon atmospheres leads to a significant widening of the band gap compared to the initial state, although again, strong differences are visible between the 700 and 900 °C samples. Notably, after the final calcination in air, the sample properties reverted to their initial state. Earlier studies have already shown that rare-earth fluorites are resistant to structural changes in this temperature range and in these atmospheres and that the crystal structure prevails.[5,29] In order to confirm this, we focused on four materials ranging from high entropy to nonentropy, which were later investigated in terms of their electronic properties. The material synthesis of $(LaTbYZrPrSmCe)O_2$, $(LaTbYZrPrSm)O_2$, $(LaTbYZrPr)O_2$, and $(LaTbYZr)O_2$ was further scaled up and

subjected to the different atmospheres described at 900 °C, as a possible structural change was expected at these temperatures. The upscaling process showed that a longer calcination time was required for the five and six component systems in order to obtain a single-phase compound, whereas the four and seven component systems formed a single phase under the synthesis conditions analogous to the high-throughput synthesis. Moreover, the crystal structure remained stable after calcinations in different atmospheres. However, we would like to point out that although the results from the literature and the testing of the materials in this work demonstrate a structure stability under different atmospheres, this may not be the case for all materials shown here. In parallel with the changes in the band gap, the optical appearance of all materials also changed, as shown in Figure S2 (Supporting Information). The reversibility of the treatment upon reheating in air and the reformation of the original band gaps become particularly visible on the samples calcinated at 700 °C, while additional regions of large band gaps appeared at 900 °C compared to 700 °C. The changes in the band gap between samples calcined in different atmospheres can be attributed mainly to the changes in the oxidation states of Pr and Tb. Studies have shown that La, Sm, and Y retain their stable +3 oxidation state while Zr and Ce remain in their +4 state. The increase in band gap energies during calcination in reducing argon atmosphere can be attributed to a reduction of Pr and Tb. In this case, the 4f levels of Pr and Tb located between O 2p and RE 5d are occupied, implying that the electronic transition from O 2p to the next unoccupied RE 5d state occurs. The charge balance due to the reduction of Pr and Tb can occur internally by the formation of oxygen vacancies or by changes in the oxidation states of the other elements. According to earlier studies on comparable materials, the formation of oxygen vacancies is responsible for the charge balance.[5,23,29]

In contrast to all other samples, the samples calcinated under argon atmosphere at 900 °C have a larger band gap than those calcinated at 700 °C. We attribute this to a stronger reduction of cations caused by a higher temperature leading to a fully occupied RE 4f state. Surprisingly, the next calcination step under 10% H_2/argon led to a slight decrease in the band gap energies in both cases (700 and 900 °C), although the reduction potential of H_2/argon is stronger than that of neat argon. However, hydrogen also can undergo quite complex chemical reactions when interacting with oxides, including the formation of H^+, H^0, and H^-, which complicates its behavior in many host materials. In general, H_2 has a strong influence on the electronic properties of materials, and it can act in two ways. It can be an amphoteric impurity leading to gap states that can result in either positive, negative or neutral charge states, or it can form a flat level at the edge of the conduction band.[40–43] In hydrogenated TiO_2 prepared by calcination of TiO_2 in a hydrogen atmosphere, a narrowing of the band gap was observed, which was attributed to the formation of a defect band near the valence band.[44] Moreover, by steadily increasing the hydrogen pressure, it was shown that the defect concentration increases with increasing hydrogen pressure, which directly affects the electronic structure. Similar behavior was observed for the incorporation of hydrogen into tungsten oxide. It was observed that the sub-stoichiometry of oxygen and the incorporation of hydrogen into tungsten oxide led to the appearance of two bands within the band gap ≈3 and ≈1 eV below the edge of the conduction band, respectively.[45] Both intermediate bands are optically active and significantly affect the optical properties of the material. The hydrogen is either incorporated into the W–O network forming O–H–O bridges, or when the material is exposed to atomic hydrogen, it is directly bound to the W ions sharing electrons with their 5d orbitals. We, therefore, assume that a similar effect controls the high- and medium-entropy materials studied in this work. To verify this, further measurements and DFT calculations would be required, but this is beyond the scope of this work.

Table 2. Selected compositions with associated band gap energies, crystal structures and configuration entropies.

Composition	Band gap	Crystal structure	S_{config}	Acronym
$(LaTbYZrPrSmCe)O_2$	2.2 eV	Single phase *Fm*-3*m*	1.95*R*	REO-7
$(LaTbYZrPrSm)O_2$	2.1 eV	Single phase *Fm*-3*m*	1.79*R*	REO-6
$(LaTbYZrPr)O_2$	2.1 eV	Single phase *Fm*-3*m*	1.61*R*	REO-5
$(LaTbYZr)O_2$	2.2 eV	Single phase *Fm*-3*m*	1.39*R*	REO-4

2.5. Other Relevant Photovoltaic Properties

From the vast combinatorial parameter space of elemental compositions, calcination temperatures, and calcination atmospheres, we have attempted to narrow the number of materials to a reasonable but promising set to make measurements in terms of photovoltaic properties. From the 64 different materials synthesized at 700 °C, we searched for compounds that met the following criteria: a) single-phase crystal structures, b) smallest band gaps in the visible spectrum, and c) with preferentially increasing configurational entropy (increasing the number of elements). The properties of these compounds, henceforth labeled REO-4 to REO-7 (describing the compounds with 4–7 different cations), are summarized in **Table 2**.

Important for their deployment in solar cells is not only their optical band gap but also their absolute energies of the conduction and valence bands. Since the materials will be incorporated into the layer stack of future solar cells, both energy levels must match the energy levels of the adjacent hole or electron extraction layers. This is particularly important, as many metal oxides (e.g., MoO_3) are notorious for very deep bands, which, if unmodified at their surface, can produce charge carrier extraction barriers. In order to characterize the transport level energies of the selected REO, we conducted measurements of their ionization potential by photoelectron spectroscopy in air (PESA). These experiments were carried out on thin-film samples that were prepared using pulsed laser deposition (PLD). The PESA data in **Figure 4** shows that all REOs exhibit IPs of 5.6 ± 0.1 eV. Within this group of REOs, we did not find a correlation between the number of incorporated cations, i.e., the entropy of the system, and the IP. Yet, the addition or removal of cationic species may well be a handle to fine-tune the IP of the REOs. The conduction band energy of the REOs can be estimated by subtraction of the optical band gap energy from the IP, yielding 3.47, 3.48, 3.46, and 3.45 eV for REO-4, REO-5, REO-6, and REO-7, respectively. Thus, both the conduction and the valence band energies exhibit a reasonable magnitude for interfacing with charge carrier transport layers.

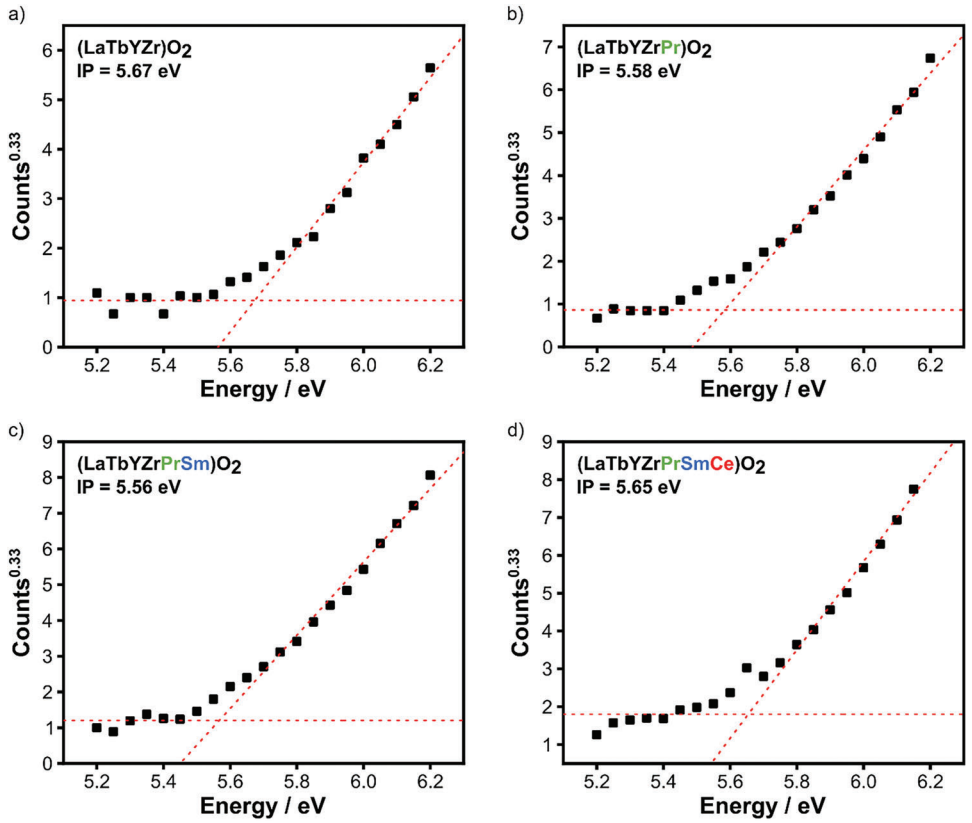

Figure 4. Measurement of the ionization potential (IP) of the REOs by PESA.

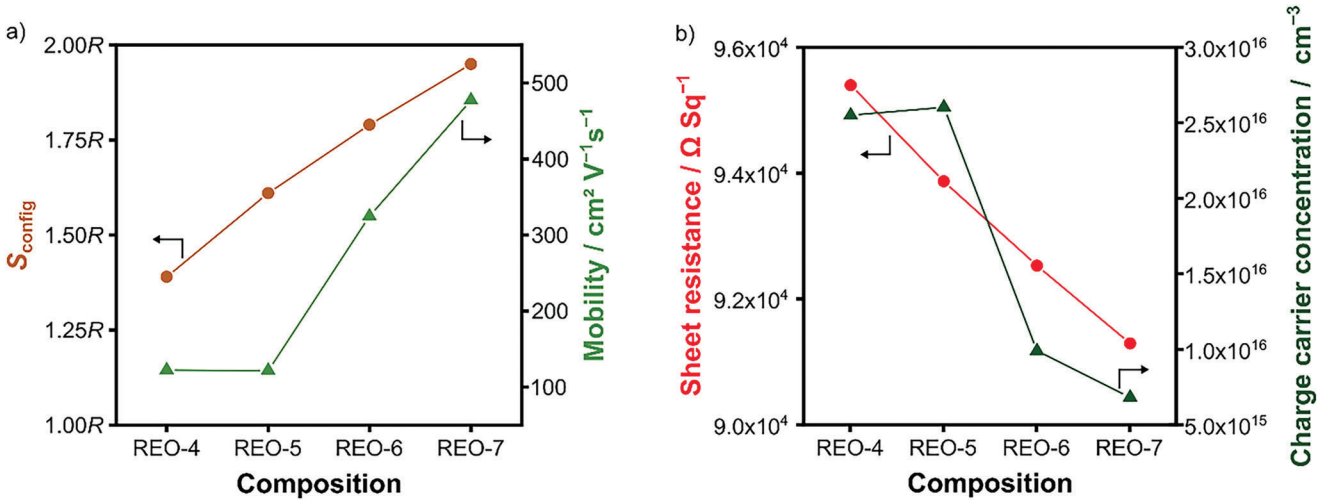

Figure 5. a) Configurational entropy and electron mobility of the different REO compounds. b) Sheet resistance and charge carrier concentration.

Finally, Hall-effect measurements were performed at room temperature to study the mobility of the charge carriers in the REOs. **Figure 5**a shows that the charge carrier mobility increases with configuration entropy, reaching a peak entropy of 477 cm^2 V^{-1} s^{-1} in REO-7. In light of the generally higher electron mobility versus hole mobility in the vast majority of (semi)conducting oxides, we interpret this data as electron mobility. At first glance, it is surprising that electron mobility increases toward compositions with higher elemental complexity since materials with high entropy often cause lattice distortions that can lead to an increased number of scattering centers for electrons. We also observed an increased mobility with larger configurational entropies, which is the result of a decreasing charge carrier concentration (Figure 5b). With the increase of mobility dominating, the sheet resistance follows the mobility trend and decreases. This behavior suggests that the optimal mobility in

the bands is reached when fewer electrons are present and that electron-electron scattering hinders charge carrier transport. A similar behavior was observed in fluorite-structured CeO_2, where doping with Ru or In also led to a decrease in charge carrier density and an increase in mobility to 583 $cm^2\ V^{-1}\ s^{-1}$.[28]

3. Conclusions

These results show that the search for promising materials in a large chemical parameter space for applications can be successfully performed with the presented high-throughput synthesis in combination with automated characterization techniques to identify potential application ranges depending on the properties of the different materials. Based on this approach, 4 material compositions with different entropy levels and compositions but comparable band gap energy (≈2 eV) were investigated for their electron mobility, which is an important parameter for potential application in photovoltaics. By using specific descriptors, the desired materials could be identified and selected from the material libraries.

In general, high-throughput synthesis and characterization methods have been used to synthesize 64 different compositions of high-entropy rare-earth oxides, most of which exhibit a single-phase fluorite structure (*Fm*-3*m*), some multi-*Fm*-3*m* structures, and very few bixbyite structures (*Ia*-3) after calcination. Automated UV–vis spectroscopy was used to characterize the band gap. Heat treatment in different atmospheres can adjust the band gaps. From the compiled material library, a series of single-phase *Fm*-3*m* compounds with increasing entropy and lowest band gaps were selected. The study revealed that high configurational entropy supports high electron mobility of REOs. Furthermore, this study demonstrates the advantages of high-throughput screening methods for material classes with an abundance of elemental and stoichiometric compositions.

4. Experimental Section

Synthesis: Water-based nitrate salt precursor solutions (0.2 mol L^{-1}) of Ce, La, Pr, Sm, Y, Zr, and Tb were prepared and used as follows:

$Ce(NO_3)_3{\cdot}6H_2O$ (Sigma-Aldrich, 99%)
$La(NO_3)_3{\cdot}6H_2O$ (Sigma-Aldrich, 99.999%)
$Pr(NO_3)_3{\cdot}6H_2O$ (ABCR, 99.9%)
$Sm(NO_3)_3{\cdot}6H_2O$ (Sigma-Aldrich, 99.9%)
$Y(NO_3)_3{\cdot}6H_2O$ (Sigma-Aldrich, 99.8%)
$ZrO(NO_3)_2{\cdot}xH_2O$ (Alfa Aesar, 99.9%)
$Tb(NO_3)_3{\cdot}6H_2O$ (ABCR, 99.9%)

In total, 64 different compositions were prepared using an automated pipetting robot (opentrons OT-2). One composition with all 7 elements, 7 compositions with 6 of the 7 elements, 21 compositions with 5 of the 7 elements, and 35 compositions with 4 of the 7 elements. In the first step, the water-based nitrate salt solutions were transferred and mixed in different combinations in a standard 360 µL 96-well plate. To initiate coprecipitation, the respective precursor solutions were mixed with ammonia (Sigma Aldrich, 28%–30%) in a ratio of 1:2 on a carrier substrate suitable for calcination and further analysis. In total, 25 µL of the desired precursor solution was deposited on each carrier substrate. Two-sided polished (100) Si wafers, Macor plates, and quartz plates were used as carrier substrates, which could be directly used for XRD, UV–vis, and SEM/EDX studies, respectively. During the entire time of coprecipitation, the respective carrier substrates were held at 70 °C. Finally, the quartz samples were dried for approximately 1 h at 70 °C. Then the samples were transferred into an oven and calcinated at either 700 or 900 °C for 6 h (heating rate 5 °C min^{-1} in air) with cooling down to room temperature inside the oven. The samples on the Macor plates were calcined again after each UV–vis examination under the same calcination conditions but different calcination atmospheres (argon, 10% H_2+argon and reheat treatment in air) to study their effect on the band gap energy.

Automated X-Ray Diffraction (XRD): Automated XRD measurements were performed at an STOE Stadi P diffractometer, equipped with a Ga-jet X-ray source (Ga-K_β radiation, 1.2079 Å) and a custom-built XY stage for automated sample measurement. XRD patterns were obtained in transmission mode. Patterns were collected between 10° and 60° 2θ with a step size of 0.02°. The powder samples on the (100) Si-wafer were fixed with Kapton folie, and the Si wafer is held by an in-house designed holder. For all the samples, a semi-automated Le Bail Fit was done using Topas Academics V5 software.

Automated Scanning Electron Microscopy (SEM) with Energy-Dispersive X-Ray Spectroscopy (EDX): A scanning electron microscope (SEM; LEO 1530, Carl Zeiss AG) with an energy dispersive X-ray spectroscopy detector (EDX; Oxford Instruments) was used to determine the chemical composition of each of the 64 samples on the quartz plate. The quartz plate was sputter coated with a 20 nm gold layer to avoid charging during EDX scanning. AZTEC software (Oxford Instruments) was used for EDX mapping (automated) and data analysis. Due to the quartz plate (SiO_2) and resulting substrate effects, the oxygen concentration was not calculated from the EDX spectra; instead, Si and O were used to deconvolve and fit the EDX spectra to determine the cation concentrations.

Automated Ultraviolet–Visible Spectroscopy (UV–vis): UV–vis spectroscopy data was collected using a Cary 60 UV–vis Spectrophotometer (Agilent) equipped with a remote fiber optic diffuse reflectance accessory and the Cary WinUV software. The baseline corrected spectra were collected between 1100 and 200 nm with a scan speed of 600 nm min^{-1}. A total of five measurements were performed on each sample. The 100% reflectance baseline was collected using a white PTFE standard. The automated measuring process is driven by an XYZ robot for sample position exchange. To prevent the measurements from being affected by light, the entire instrument is housed in a black box.

Determination of Band Gaps: The band gap energies were determined automatically from the UV–vis spectra using the Tauc plot method, which is based on the relationship between band gap energy (E_g) and reemission function $F(R_\infty)$, also known as the Kubelka–Monk function. The band gap energy is obtained by extrapolating the intersection of the linear region of the Tauc plot versus the photon energy. For more details on UV–vis analysis, the reader is referred to references.[5,16] A Python model was developed for the band gap energy evaluation. The developed algorithm for automated data evaluation consists of five steps: data preprocessing, piecewise linear fitting, baseline identification, linear segment identification, and band gap energy estimation. After preprocessing the data, a piecewise linear fit was performed using a Python-based library (pwlf) with a quality value (R-squared) greater than 99.95%. Using this piecewise linear fit, the slopes and breakpoints are evaluated. The baseline was determined based on the slope of the line being less than 3°, and the linear segment was analyzed as the linear region having an *R*-squared fit greater than 99.50% and an angle greater than the slope of the baseline. It was taken into account that the linear segment is neither the first nor the last line among all matched lines. The minimum length of the linear segment was set to 0.25 eV as a limit.

Photoelectron Spectroscopy in Air (PESA): PESA data were collected using an AC-2 spectrometer (Riken Keiki Co. Ltd, Japan) on thin films of the following high-entropy materials: $(LaTbYZr)O_2$, $(LaPrTbYZr)O_2$, $(LaPrSmTbYZr)O_2$, and $(CeLaPrSmTbYZr)O_2$. For this purpose, the HEO synthesis was scaled up using coprecipitation, as described in the section on high-throughput synthesis. The powders were compressed under a pressure of 3 tons and sintered at 1200 °C. Then, 200 nm thick films were deposited by pulsed laser deposition (PLD) on silicon wafers using a laser fluence of 1.72 J cm^{-2} and a frequency of 5 Hz at an oxygen pressure of 0.05 mbar. The temperature of the substrates was maintained at 700 °C during deposition. The distance between the samples and the targets was 2.5 cm, and the size of the laser spot was 0.04 mm^2. The aperture for laser

input during PLD was kept at 7 mm. After deposition, the samples were annealed in the PLD chamber at 700 °C and 100 mbar oxygen pressure for 15 minutes.

In the PESA measurement, monochromatic UV photons with an intensity of 1500 nW were used to excite the photoelectrons on the sample surface. The photon energy was increased stepwise by 0.05 eV. The measurement was performed in the range of 5.2–6.2 eV, and the integration time was 10 s.

Hall Measurements: Hall measurements were done using an HCS10 Hall Effect Measurement System (Linseis Messgeräte GmbH, Germany). Measurements were made at room temperature in a Magnet field varying from −0.5 to 0.5 T at an applied current of 0.0009 mA. Data analysis was performed using the Van der Pauw method.

Supporting Information

Supporting Information is available from the Wiley Online Library or from the author.

Acknowledgements

M.K. and A.K. contributed equally to this work. S.S. acknowledges the support from the EPISTORE project funded by the European Union's Horizon 2020 research and innovation program under grant agreement no. 101017709. A.K., A.C., and B.B. acknowledge funding by the Carl-Zeiss Foundation, project KeraSolar. H.H. is grateful for support from the Deutsche Forschungsgemeinschaft under grant HA1344/43-2. The authors thank Holger Röhm and Christian Sprau for their continuous support.

Open access funding enabled and organized by Projekt DEAL.

Conflict of Interest

The authors declare no conflict of interest.

Data Availability Statement

The data that support the findings of this study are available from the corresponding author upon reasonable request.

Keywords

Hall-effect measurements, high-entropy materials, High-throughput, multicomponent materials, photoelectron spectroscopy in atmosphere, UV–vis

Received: December 21, 2022
Revised: March 24, 2023
Published online: May 4, 2023

[1] J. Wang, Y. Cui, Q. Wang, K. Wang, X. Huang, D. Stenzel, A. Sarkar, R. Azmi, T. Bergfeldt, S. S. Bhattacharya, R. Kruk, H. Hahn, S. Schweidler, T. Brezesinski, B. Breitung, *Sci. Rep.* **2020**, *10*, 18430.
[2] D. Bérardan, S. Franger, D. Dragoe, A. K. Meena, N. Dragoe, *Phys. Status Solidi RRL* **2016**, *10*, 328.
[3] C. Duan, X. Li, D. Wang, Z. Wang, H. Sun, R. Zheng, Y. Liu, *Sustainable Energy Fuels* **2022**, *6*, 1479.
[4] S. Jiang, T. Hu, J. Gild, N. Zhou, J. Nie, M. Qin, T. Harrington, K. Vecchio, J. Luo, *Scr. Mater.* **2018**, *142*, 116.
[5] A. Sarkar, B. Eggert, L. Velasco, X. Mu, J. Lill, K. Ollefs, S. S. Bhattacharya, H. Wende, R. Kruk, R. A. Brand, H. Hahn, *APL Mater.* **2020**, *8*, 051111.
[6] R. Djenadic, A. Sarkar, O. Clemens, C. Loho, M. Botros, V. S. K. Chakravadhanula, C. Kübel, S. S. Bhattacharya, A. S. Gandhi, H. Hahn, *Mater. Res. Lett.* **2017**, *5*, 102.
[7] A. Sarkar, R. Djenadic, D. Wang, C. Hein, R. Kautenburger, O. Clemens, H. Hahn, *J. Eur. Ceram. Soc.* **2018**, *38*, 2318.
[8] Y. Ma, Y. Ma, Q. Wang, S. Schweidler, M. Botros, T. Fu, H. Hahn, T. Brezesinski, B. Breitung, *Energy Environ. Sci.* **2021**, *14*, 2883.
[9] L. Lin, K. Wang, A. Sarkar, C. Njel, G. Karkera, Q. Wang, R. Azmi, M. Fichtner, H. Hahn, S. Schweidler, B. Breitung, *Adv. Energy Mater.* **2022**, *12*, 2103090.
[10] D. Stenzel, B. Zhou, C. Okafor, M. V. Kante, L. Lin, G. Melinte, T. Bergfeldt, M. Botros, H. Hahn, B. Breitung, S. Schweidler, *Front. Energy Res.* **2022**, *10*, 942314.
[11] B. Petrovičovà, W. Xu, M. G. Musolino, F. Pantò, S. Patanè, N. Pinna, S. Santangelo, C. Triolo, *Appl. Sci.* **2022**, *12*, 5965.
[12] G. H. J. Johnstone, M. U. González-Rivas, K. M. Taddei, R. Sutarto, G. A. Sawatzky, R. J. Green, M. Oudah, A. M. Hallas, *J. Am. Chem. Soc.* **2022**, *144*, 20590.
[13] C. M. Rost, E. Sachet, T. Borman, A. Moballegh, E. C. Dickey, D. Hou, J. L. Jones, S. Curtarolo, J. P. Maria, *Nat. Commun.* **2015**, *6*, 8485.
[14] B. S. Murty, J. W. Yeh, S. Ranganathan, P. P. Bhattacharjee, *High-Entropy Alloys*, Elsevier Science, Amsterdam **2019**.
[15] L. J. Santodonato, P. K. Liaw, R. R. Unocic, H. Bei, J. R. Morris, *Nat. Commun.* **2018**, *9*, 4520.
[16] L. Velasco, J. S. Castillo, M. V. Kante, J. J. Olaya, P. Friederich, H. Hahn, *Adv. Mater.* **2021**, *33*, 2102301.
[17] X. D. Xiang, X. Sun, G. Briceño, Y. Lou, K. A. Wang, H. Chang, W. G. Wallace-Freedman, S. W. Chen, P. G. Schultz, *Science* **1995**, *268*, 1738.
[18] A. Ludwig, R. Zarnetta, S. Hamann, A. Savan, S. Thienhaus, *Z. Met. Res. Adv. Tech.* **2008**, *99*, 1144.
[19] E. McCalla, M. Parmaklis, S. Rehman, E. Anderson, S. Jia, A. Hebert, K. Potts, A. Jonderian, T. Adhikari, M. Adamic, *Can. J. Chem.* **2022**, *100*, 132.
[20] T. Adhikari, A. Hebert, M. Adamič, J. Yao, K. Potts, E. McCalla, *ACS Comb. Sci.* **2020**, *22*, 311.
[21] F. Lourens, A. Ludwig, *Surf. Coat. Technol.* **2022**, *449*, 128984.
[22] A. Frantzen, J. Scheidtmann, G. Frenzer, W. F. Maier, J. Jockel, T. Brinz, D. Sanders, U. Simon, *Angew. Chem., Int. Ed.* **2004**, *43*, 752.
[23] A. Sarkar, C. Loho, L. Velasco, T. Thomas, S. S. Bhattacharya, H. Hahn, R. Djenadic, *Dalton Trans.* **2017**, *46*, 12167.
[24] Y. Lin, C. Xu, J. Ren, X. Qu, *Angew. Chem., Int. Ed.* **2012**, *51*, 12579.
[25] S. Zhang, C. Zhao, Y. Liu, W. Li, J. Wang, G. Wang, Y. Zhang, H. Zhang, H. Zhao, *Chem. Commun.* **2019**, *55*, 2952.
[26] A. Shinde, G. Li, L. Zhou, D. Guevarra, S. K. Suram, F. M. Toma, Q. Yan, J. A. Haber, J. B. Neaton, J. M. Gregoire, *J. Mater. Chem. A* **2016**, *4*, 14356.
[27] T. Audichon, S. Morisset, T. W. Napporn, K. B. Kokoh, C. Comminges, C. Morais, *ChemElectroChem* **2015**, *2*, 1128.
[28] R. Rangel, L. Chávez-Chávez, E. Martínez, P. Bartolo-Pérez, *Phys. Status Solidi Basic Res.* **2012**, *249*, 1199.
[29] A. Sarkar, P. K. Mannava, L. Velasco, C. Das, B. Breitung, S. S. Bhattacharya, R. Kruk, H. Hahn, *Scr. Mater.* **2022**, *207*, 114273.
[30] N. M. Jacob, G. Madras, N. Kottam, T. Thomas, *Ind. Eng. Chem. Res.* **2014**, *53*, 5895.
[31] K. Ahn, D. S. Yoo, D. H. Prasad, H. W. Lee, Y. C. Chung, J. H. Lee, *Chem. Mater.* **2012**, *24*, 4261.
[32] R. O. Yathisha, Y. Arthoba Nayaka, *J. Mater. Sci.* **2018**, *53*, 678.
[33] Y. Xu, X. Hao, X. Zhang, T. Wang, Z. Hu, Y. Chen, X. Feng, W. Liu, F. Hao, X. Kong, C. He, S. Ma, B. Xu, *CrystEngComm* **2022**, *24*, 3369.

[34] H. Xie, H. Wang, Q. Geng, Z. Xing, W. Wang, J. Chen, L. Ji, L. Chang, Z. Wang, J. Mao, *Inorg. Chem.* **2019**, *58*, 5423.
[35] P. Erhart, K. Albe, A. Klein, *Phys. Rev. B: Condens. Matter Mater. Phys.* **2006**, *73*, 205203.
[36] Y. K. Kuo, B. Ramachandran, C. S. Lue, *Front Chem* **2014**, *2*, 1.
[37] Y. Zhydachevskyy, Y. Hizhnyi, S. G. Nedilko, I. Kudryavtseva, V. Pankratov, V. Stasiv, L. Vasylechko, D. Sugak, A. Lushchik, M. Berkowski, A. Suchocki, N. Klyui, *J. Phys. Chem. C* **2021**, *125*, 26698.
[38] M. Setvín, M. Wagner, M. Schmid, G. S. Parkinson, U. Diebold, *Chem. Soc. Rev.* **2017**, *46*, 1772.
[39] I. P. Raevski, S. M. Maksimov, A. V. Fisenko, S. A. Prosandeyev, I. A. Osipenko, P. F. Tarasenko, *J. Phys. Condens. Matter* **1998**, *10*, 8015.
[40] H. Li, J. Robertson, *J. Appl. Phys.* **2014**, *115*, 203708.
[41] C. G. Van De Walle, *Phys. Rev. Lett.* **2000**, *85*, 1012.
[42] Ç. Kiliç, A. Zunger, *Appl. Phys. Lett.* **2002**, *81*, 73.
[43] P. W. Peacock, J. Robertson, *Appl. Phys. Lett.* **2003**, *83*, 2025.
[44] L. Bin Mo, Y. Bai, Q. Y. Xiang, Q. Li, J. O. Wang, K. Ibrahim, J. L. Cao, *Appl. Phys. Lett.* **2014**, *105*, 202114.
[45] M. Vasilopoulou, I. Kostis, N. Vourdas, G. Papadimitropoulos, A. Douvas, N. Boukos, S. Kennou, D. Davazoglou, *J. Phys. Chem. C.* **2014**, *118*, 12632.